# Evaluation of the Fracture Toughness of a SMSS Subjected to Common Heat Treatment Cycles in an Aggressive Environment

*G. Pieta, R. Leite, C. Kwietniewski, T. Clarke, and T. Strohaecker*

*(Submitted January 15, 2010)*

**Supermartensitic stainless steels (SMSS) are an alternative to corrosion-prone carbon steels and expensive duplex stainless steels in offshore tubing applications for the oil and gas industry. Due to their differentiated alloying, SMSS exhibit superior toughness, corrosion resistance, and weldability properties when compared with another viable option, conventional martensitic stainless steels. However, when cathodically protected in a seawater environment they can be susceptible to embrittlement due to hydrogen charging. In the present study, SMSS samples were removed from deep water pipelines and their fracture toughness in the as-received condition and with different heat treatments was evaluated. Tests were carried out in air and in harsh environmental and loading conditions, which were ensured by subjecting specimens to cathodic overprotection, simulating effects seen in structures with complex geometries, and to incremental step loads in a synthetic seawater environment, thus favoring hydrogen diffusion to the precrack tip. The fracture surfaces of the specimens were analyzed in order to identify hydrogen-induced embrittlement and fracture toughness values of specimens tested in air were compared to values obtained in environment-assisted experiments. The influence of microstructure was evaluated by control of the retained austenite and δ-ferrite contents of the specimens. The results show a significant drop in the fracture toughness of steel in the studied environment, with a fracture mode which is clearly more brittle and dependent on microstructural characteristics of the samples.**

---

| **Keywords** | cathodic protection, fracture toughness, hydrogen embrittlement, seawater environment, supermartensitic stainless steels (SMSS) |
|---|---|

## 1. Introduction

Supermartensitic stainless steels (SMSS) are a variation of the traditional 13% Cr martensitic steel, with lower carbon content and additional nickel and molybdenum alloying, which enhances of their weldability and mechanical properties (Ref 1-4). Furthermore, their relatively lower cost makes them an attractive option as a substitute for more expensive duplex and superduplex stainless steels, and their use in offshore deep water tubing applications has increased significantly in recent years (Ref 2, 5).

Even though their differentiated chemical composition ensures an improved corrosion resistance in $CO_2$ and high chloride content environments in comparison with traditional 13% Cr martensitic steel (Ref 6), operation in deep waters can lead to pitting corrosion particularly if chromium-precipitates

are formed due to inadequate heat treatment (Ref 7). Cathodic protection is commonly used on steels in such environments, but this can lead to hydrogen charging and consequent embrittlement (Ref 8). The permeation of hydrogen in SMSS as a function of microstructure and pH values has been evaluated in (Ref 9, 10) and the effect of hydrogen on the location of the rupture of welded SMSS specimens in slow strain uniaxial tests was shown in (Ref 11). In Olsen and Hesjevik (Ref 12), results from similar slow strain tests in harsh environments are given, but the authors also established that tests in more severe loading conditions were essential to determine fracture behavior in realistic conditions. Limited literature is indeed available on the effect of hydrogen embrittlement on the fracture toughness of SMSS in demanding stress corrosion conditions. Furthermore, structural integrity of offshore oil extraction equipment in a country like Brazil is paramount, since 80% of its oil comes from such an environment; it is therefore necessary to evaluate such steels in real service conditions.

In the present study, SMSS precracked specimens in the as-received condition, and with two different heat treatments, were step loaded over several days in a synthetic seawater environment; the different conditions were studied in order to evaluate the effect of varying microstructural characteristics, such as the δ-ferrite and retained austenite contents, on the mechanical resistance of the steels in such an environment. During these tests an overprotection potential was applied to the specimens in order to simulate a localized level of cathodic protection which can occur in real operation conditions, especially due to structure complexities or poor operational procedures (Ref 13). Step loading tests are a quick and rugged

**G. Pieta, R. Leite, C. Kwietniewski, T. Clarke,** and **T. Strohaecker**, Post-Graduation Program in Mining, Metallurgical and Materials Engineering (PPGEM), Federal University of Rio Grande do Sul (UFRGS), Av. Osvaldo Aranha, 99, Sala 610, Porto Alegre, RS, Brazil. Contact e-mails: tclarke@demet.ufrgs.br and thomas.clarke05@imperial.ac.uk

way of obtaining information on the fracture toughness of specimens, and when performed as an environment-assisted test they simulate severe service conditions due to the extended times given for hydrogen to reach the crack tip. The results were compared with those obtained from fracture toughness tests in air, and the fracture regime of the specimens in environmental tests was investigated by analysis of the near crack tip region by Scanning Electron Microscopy (SEM); this was used in an attempt to identify the occurrence of plastic deformation before crack propagation (Ref 14). The approach presented here can be useful as a technique for evaluation of specimens in immersion tests where the use of clip gauges is complicated, either due to the high cost of such sensors or to space limitations in the environment chamber, and in cases where only specimens of limited size are available.

## 2. Materials and Methods

Optical Emission Spectrometry was used to obtain the chemical composition of the high alloyed SMSS used in this study, and results are presented in Table 1. To ensure that realistic samples were being obtained, material was removed directly from a seamless pipeline with wall thickness of approximately 12.7 mm, from which compact tension (CT) specimens were produced according to (Ref 15), with the notch aligned with the rolling (axial) direction of the pipe. The number and allocation of samples were carefully selected due to the restricted amount of material available. Five samples were kept in the as-received condition (condition 1), which had an unknown heat treatment history. Ten specimens suffered austenitization at 1000 °C for 40 min and then were air cooled and then tempered once at 670 °C for 1 h 30 min and air cooled (condition 2); five of these were then tempered once more at 600 °C at 1 h 30 min (condition 3). Microstructural characterization of all samples was performed using standard metallographic practice and Optical Microscopy, and the amount of δ-ferrite in the specimens was estimated with the image analysis software Image-J, the final volumetric percentage presented being an average of five images on each sample. Specimens were also analyzed by x-ray diffraction in a Philips X'Pert MPD Diffractometer, using a Cu-Kα radiation tube operating at 40 kV and 50 mA. These spectrograms were used to calculate the volumetric percentage of retained austenite in the samples by the direct comparison method as in, for example, (Ref 16, 17); in this article the chosen peaks were the (110) for martensite and the (111) for austenite. The system was

operated under a θ-2θ geometry, and was used to cover a degree range from 47° to 103° in 0.05° increments. The SMSS mechanical properties were further evaluated by Vickers microhardness.

Fracture toughness tests were conducted at room temperature in air and in a synthetic seawater environment. Air tests were carried out by submitting three specimens of each condition to monotonic loading up to fracture using a MTS 810 machine, with a clip-gauge being used to measure crack mouth opening displacement (Ref 18). The fracture toughness environment-assisted tests were carried out by submitting two precracked CT specimens for each condition (also prepared according to Ref 15) to increasing tensile load steps up to fracture while exposed to a synthetic water environment, prepared according to (Ref 19). Cathodic protection was applied by an impressed current at the potential of $-1100$ mV$_{SCE}$, simulating an overprotection condition. Three load steps of 5 MPa $\cdot \sqrt{m}$, followed by a number of 1 MPa $\cdot \sqrt{m}$ steps, were applied until specimen fracture by a system of dead weights, and a load cell was used for control. Each load step was kept constant for 24 h. The tests provided $K$ values which allowed a comparison between SMSS fracture behavior in air and in the studied environment. Analysis of the fractured CT specimens was carried out by Scanning Electron Microscopy (SEM) in order to obtain information about the fracture micro-mechanisms involved in each case.

## 3. Results

### 3.1 Material Characterization

Figure 1a shows the microstructure of an SMSS sample in the as-received condition, which consists of tempered lath martensite with a considerable amount of precipitates; only this microstructure will be shown in this work since microstructures of heat-treated specimens have a similar macroscopic aspect. Precipitates in high alloyed SMSS can be of several forms: those which cause the greatest concern are molybdenum and chromium carbonitrites, the latter being especially detrimental to the corrosion properties of the steel. Relatively high contents of titanium are added to the alloy in order to prevent chromium and molybdenum carbonitride formation, leading to the precipitation of Ti(C,N) compounds (Ref 20). Furthermore, relatively high levels of nickel are necessary to promote martensite phase in the SMSS microstructure, due to its role in austenite stabilization; some intermetallic compounds such as TiNi are therefore also likely to be formed, and these may induce a secondary hardening effect as described in Kondo et al. (Ref 21).

Samples received an electrolytic treatment to reveal the presence of δ-ferrite in the matrix; as an example, Fig. 1(b) shows the microstructure of an as-received sample. Specimens of all states received such metallographic treatment and were used in calculations of the percentage amount of this phase by image analysis. X-ray diffraction analyses were carried out on the SMSS specimens, and the presence of some austenite in the martensitic matrix of the steel specimens was identified in all cases. As an example, a XRD pattern of one of the SMSS samples in the as-received condition is shown in Fig. 2.

Material characterization results are summarized in Table 2, along with data from fracture toughness tests, as a basis for the

**Table 1  Chemical composition of studied SMSS**

| Element | % mass | Element | % mass |
|---------|--------|---------|--------|
| C  | 0.013 | Nb | 0.012 |
| Cr | 12.95 | Ti | 0.4 |
| Ni | 5.21  | V  | 0.12 |
| Mo | 2.02  | W  | 0.017 |
| Si | 0.29  | P  | 0.021 |
| Mn | 0.48  | S  | <0.001 |
| Al | 0.05  | Pb | <0.002 |
| Co | 0.06  | Sn | 0.007 |
| Cu | 0.12  | Fe | Bal. |

discussions in Section 4. Specimens in condition 1 had a percentage of δ-ferrite of 8.4% in volume, which is considerably high for these steels. These specimens also had 2.8% in volume of retained austenite, and an average Vickers hardness of 307 Hv. Specimens in condition 2 suffered a reduction in δ-ferrite content, to 7.2% in volume; slight increases in the retained austenite (3%) content and average hardness, to 331 Hv, were also observed. The volumetric content of δ-ferrite was similar for specimens in condition 3 (7.3%), but the volume of retained austenite was reduced to 1.5%, which led to an increase in hardness to 341 Hv.
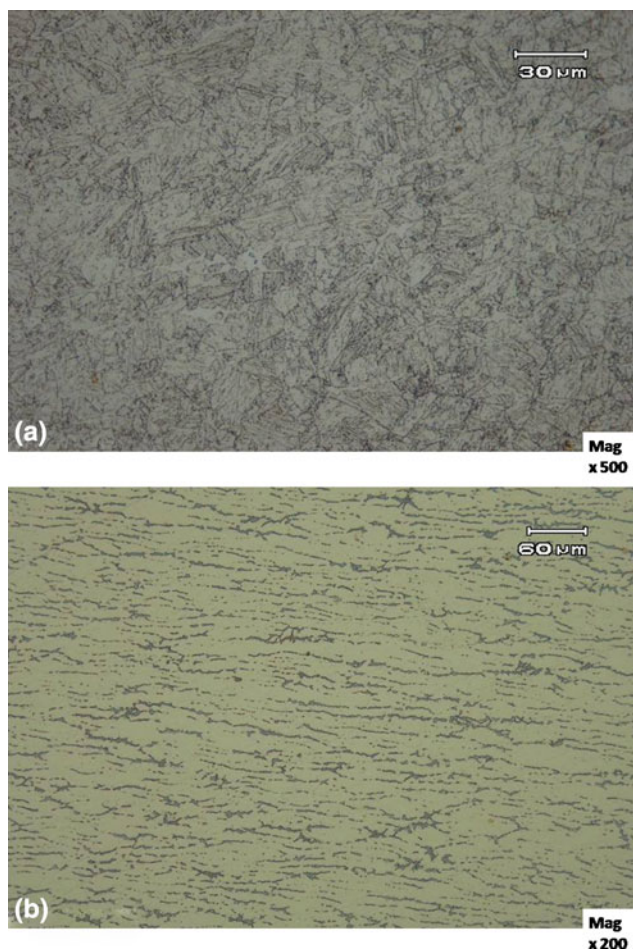


**Fig. 1** SMSS microstructures in the as-received condition (optical microscopy); (a) Martensitic matrix with precipitates. Etchant: Villella's reagent. Mag. 500×; (b) δ-ferrite distribution (*light grey*). Etchant: electrolytic KOH. Mag. 200×

### 3.2 Fracture Toughness in Air

Figure 3 shows the stress intensity factor versus crack mouth opening displacement plots, obtained from one sample of each of the three conditions tested in air. A significant ductile behavior is seen in all cases, all fractures being within the plastic regime. Because of the type of fracture, the value of the CTOD parameter at maximum load was established as the fracture toughness parameter in air, as determined by (Ref 18), average values being 0.33, 0.37, 0.36 mm for conditions 1, 2, and 3, respectively. Moreover, to compare the fracture mechanisms in air with those in environment-assisted tests, the maximum $K$ values obtained in the monotonic tests in air were defined as $K_{apparent}$, as indicated by (Ref 18). Average values of $K_{apparent}$ were of 128, 134, and 127 MPa·√m for conditions 1, 2, and 3, respectively (see Table 2 for summarized results). Post-mortem SEM analysis of the fracture surfaces of the samples showed little difference between the fracture modes of samples in the different states, all displaying a fracture mode by microvoid coalescence, as shown in Fig. 4(a) for an as-received sample, and in Fig. 4(b) for a quenched and tempered sample (condition 2). Such appearance may be attributed to the existence of internal interfaces between the matrix and austenite particles and precipitates, which may act as voiding nucleation sites (Ref 4). This ductile fracture mechanism confirms fracture in the elastic-plastic regime with significant plastic strain. The macroscopic analysis of the specimens also showed a clearly ductile fracture, with angular edges at the fracture surfaces, as can be seen in the photographs in Fig. 4.

### 3.3 Environment-Assisted Fracture Toughness

Table 2 shows values of $K$ at fracture obtained from environment-assisted tests under step loading conditions, which
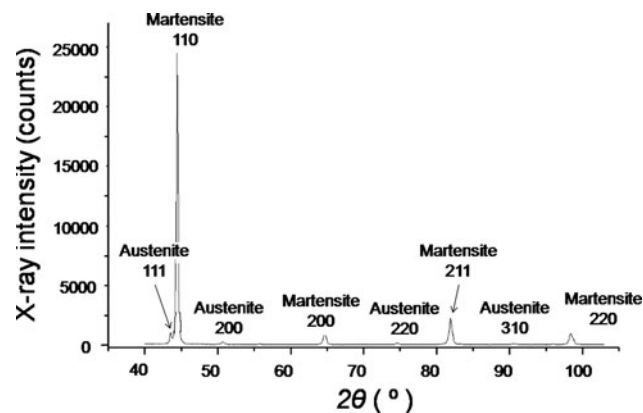


**Fig. 2** XRD pattern of SMSS in the as-received condition

**Table 2  Results from tests on SMSS specimens in different heat treatment conditions**

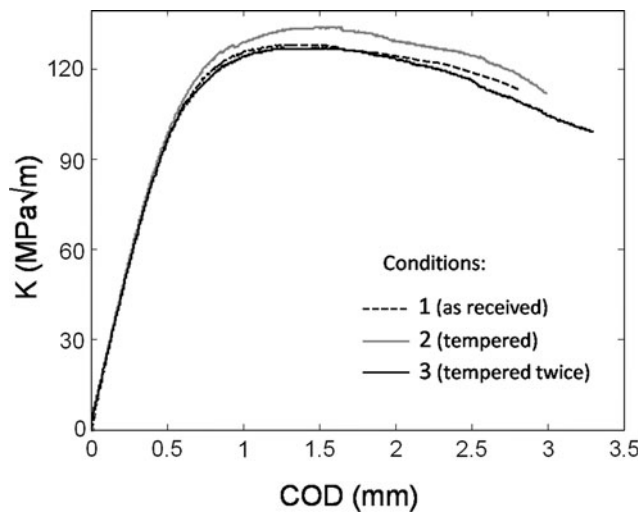| | Condition | Hardness, Hv | Austenite, vol.% | δ-ferrite, vol.% | CTOD at max. load | $K_{max}$ ($K_{apparent}$), MPa·√m | $K_{fracture}$ ($K_{IEAC}$), MPa·√m |
|---|---|---|---|---|---|---|---|
| 1. | As-received | 307 | 2.8 | 8.2 | 0.33 | 128 | 56 |
| | | | | | | | 61 |
| 2. | Quenched and tempered | 331 | 3 | 7.2 | 0.37 | 134 | 26 |
| | | | | | | | … |
| 3. | Quenched and double tempering | 341 | 1.5 | 7.3 | 0.36 | 127 | 25 |
| | | | | | | | 27 |

**Fig. 3** Stress concentration factor for samples with different heat treatment as a function of crack opening displacement resulting from fracture toughness tests in air



**Fig. 4** SEM image of fracture surface after fracture toughness test in air revealing a ductile fracture by dimples for samples, and macroscopic aspect of ruptured sample, in the: (a) as-received condition, Mag. 270×; (b) quenched and tempered condition, Mag. 270×

were performed in duplicate for each of the heat treatment states. Only one value was obtained for condition 2 because of imperfect growth of the fatigue precrack and the limited amount of material available did not allow a substitute specimen to be produced. Fracture toughness values for the heat-treated specimens are less than half of the value obtained for the as-received condition. Post-mortem SEM analysis of the fracture surfaces showed a quasi-cleavage fracture mode for the as-received specimen, as shown in Fig. 5(a), and a predominantly intergranular fracture mode with regions of quasi-cleavage for the heat-treated specimens, as shown in Fig. 5(b) for condition 3. Macroscopic analysis of specimens after rupture showed that the fracture of both specimens was fragile, with a clearly rectangular fracture surface and sharp edges up to the final tearing of the sample, as seen in photographs in Fig. 5. Furthermore, strong pitting corrosion was seen in the specimens in condition 3, as indicated by the circles in Fig. 5(b).

## 4. Discussion

The first step after data collection was to quantify the reduction of fracture toughness of samples in environment-assisted tests in relation to those tested in air. Traditionally, this can be performed by comparison of measured CMOD values in both tests, which requires a relatively more sophisticated instrumentation system consisting of sealed and corrosion resistant clip-gauges, or alternatively by direct comparison of stress concentration factor values obtained from both tests; this can be a simpler, cheaper, and more rugged solution, provided it is performed correctly and in a controlled manner which includes validating the $K$ ambient values given in Table 2 as being equivalent to $K_{IEAC}$ for each case. If performed according to (Ref 22), fracture toughness tests using the step loading technique allow direct determination of $K_{IEAC}$ values for the evaluated material in a specific environment. However, for these values to be valid, the specimens must attend a certain minimum thickness which ensures that a plane strain state is
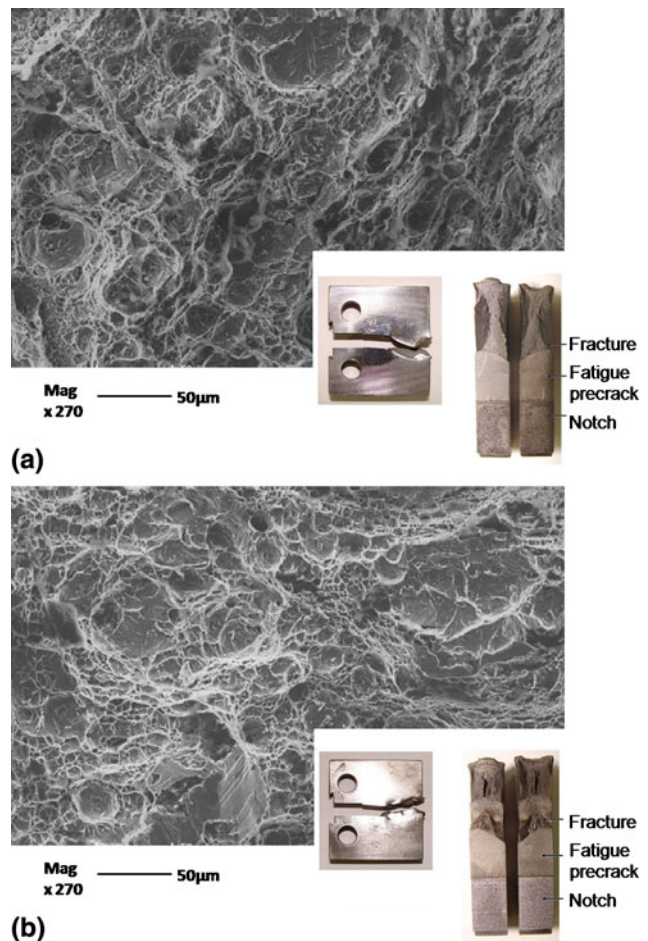
obtained at the crack tip. As mentioned in Section 2, CT specimens were produced directly from the pipeline of interest in order to guarantee that they were as realistic as possible, even though this also meant that the maximum allowable thickness of these specimens was less than that needed to allow direct determination of valid $K_{IEAC}$ parameters, as indicated in (Ref 22).

However, as is shown as an example in Fig. 6(a) for the as-received condition, analysis of the fracture surface for all the environment-assisted tests showed the absence of a stretched zone at the crack propagation front; Fig. 6(b) shows a similar analysis of the a specimen in the as-received condition when fractured in air, which shows the clear presence of such a stretched zone between the fatigue precrack and the fracture surface. Stretched zones are characteristic of fractures in the elastic-plastic regime and are formed by coarse slip steps during the crack blunting process; this means that a large amount of plastic strain has occurred before the formation and coalescence of voids lead to rupture (Ref 23). Hence, the fracture in Fig. 6(a) shows that a plane strain state was achieved and supports the assessment that fracture in the particular conditions of this environment-assisted test occurred in the linear elastic regime; the values of $K$ at fracture given in Table 2 can therefore assumed to be the $K_{IEAC}$ values for the SMSS
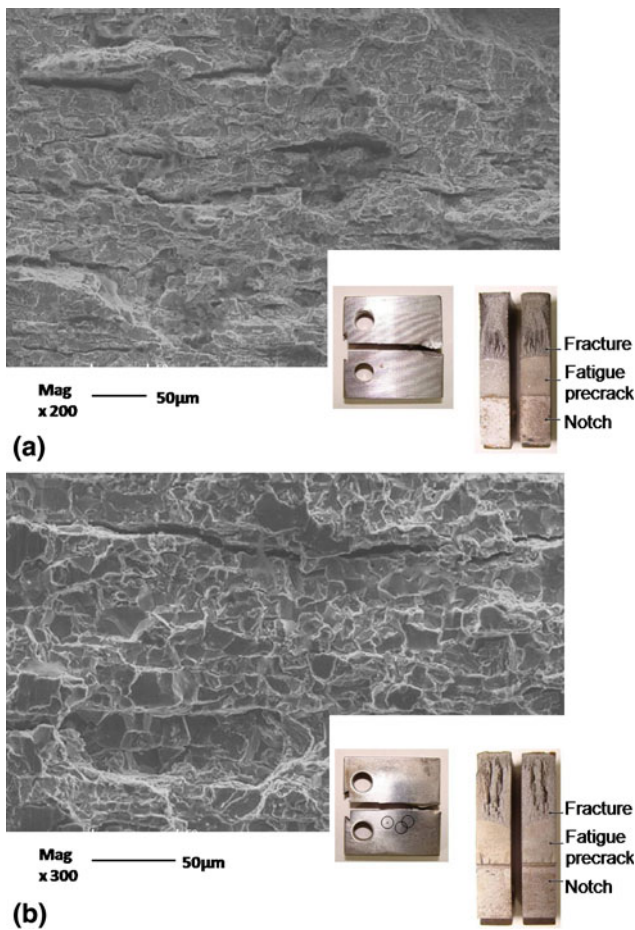
**Fig. 5** (a) SEM image of fracture surface of sample and macroscopic ruptured sample in the as-received condition after ambientassisted step loading test, showing a quasi-cleavage brittle fracture mode, Mag. 200×; (b) SEM image of fracture surface of sample and macroscopic ruptured sample in the quenched and double tempered condition after ambient-assisted step loading test, showing a predominantly intergranular brittle fracture mode, Mag. 300×



**Fig. 6** SEM image of fracture surface of sample in the as-received condition after: (a) environment-assisted fracture toughness test, showing the absence of a stretched zone. Mag. 80×; (b) test in air, showing the presence of a stretched zone between the fatigue crack and the ductile fracture. Mag. 100×

specimens in this particular case. No evidence of stretched zones were found in any of the specimens used in environment-assisted tests, heat-treated samples included; this was expected since these specimens exhibited a considerably lower $K$ value in comparison with the as-received condition.

Analysis of the results in Table 2 can also reveal some details of the influence of the microstructure of the different heat treatment conditions on the fracture toughness of SMSS. Figure 3 shows that for tests in air the stress concentration factor versus CMOD curve for samples in condition 3 are very close to the curves for condition 1, whereas the curve for condition 2 shows higher values of stress concentration factor; even though the fracture mode in all cases is similar, as seen in Fig. 4, the curve for condition 2 samples suggests a relative higher ductility of this state which may be explained by the combination of low percentage volume values of fragile δ-ferrite and high percentage volume values of ductile retained austenite. The influence of retained austenite as an independent factor can be identified from data in Table 2; when its content is reduced by half from condition 2 to 3, a decrease in ductility is clearly seen as expressed by the higher hardness, caused by the
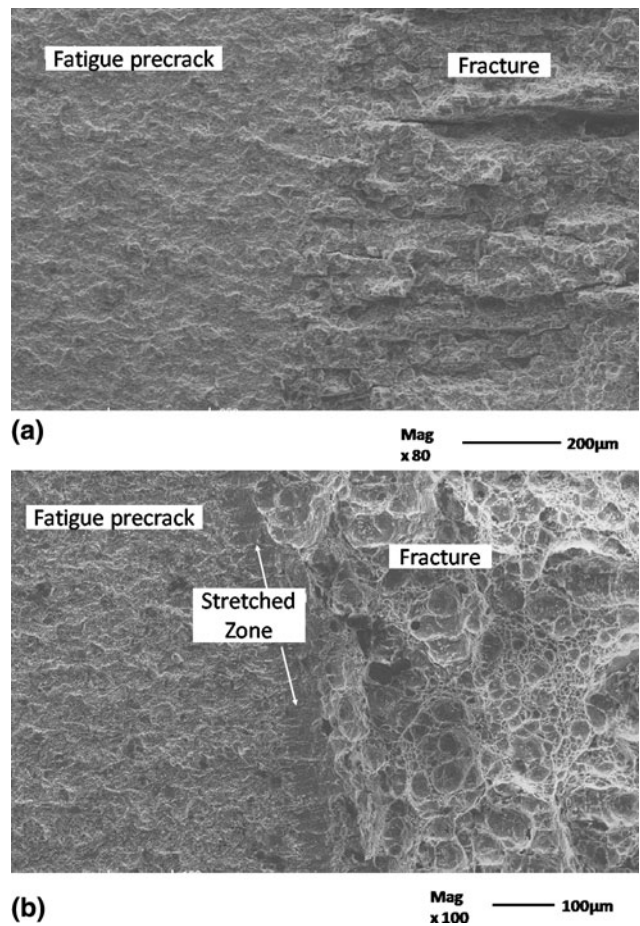
transformation to martensite, and lower stress concentration values (in Fig. 3) of the latter. The effect of δ-ferrite is not so easily identified; the reduction in its content from condition 1 to 2 could be responsible for the increase in ductility observed, but the higher hardness values of samples in condition 2 suggest a counter balancing effect caused by the increase in martensite content, even though the martensite formed in steels with such low carbon content is relatively soft (Ref 24); the mechanical properties of this condition are also influenced by the slight increase in retained austenite which is seen in the table.

Results in Table 2 may also explain the different fracture modes seen in Fig. 5 for specimens in the as-received and heat-treated conditions. It was shown in Viyanit (Ref 25) that if formation of δ-ferrite is to be avoided, chromium content should be kept below 12% for Fe-C-Cr alloys since this is the limit between the austenite and austenite + δ-ferrite field in the Fe-Cr phase diagram of an alloy with 0.01% mass of carbon. The high chromium content in this SMSS, above 12% as seen in Table 1, may explain the relatively high contents of δ-ferrite seen in Table 2. The decrease in the content of δ-ferrite from condition 1 to 2 and 3, suggests that more austenite was formed during austenitization of samples, which could be a consequence of a reduction in chromium content in the matrix. It was

shown in Park and Park (Ref 26) that chromium-rich $M_{23}C_6$ carbides may form during austenitization, and it has been shown in (Ref 27, 28) that precipitation of chromium carbides in the grain boundaries can lead to sensitization of these areas and to intergranular brittle fractures such as those seen in Fig. 5. The pitting corrosion seen in the samples in condition 3 (at the position of the circles in Fig. 5b) also indicates that sensitization has indeed occurred. These carbides were characterized in (Ref 27) by Scanning Tunneling Microscopy and shown to have a diameter of around 10 nm; the total volume of carbides is therefore relatively insignificant compared to other phases, making the confirmation of the presence of these compounds by other techniques difficult.

Precipitation of carbides at grain boundaries also increases the hydrogen embrittlement effect in these steels as shown in Gonzalez-Rodriguez et al. (Ref 29), since these, along with dislocations, are trap sites for hydrogen; this would explain the far lower fracture toughness of the heat-treated specimens in comparison with the as-received condition. Nevertheless, hydrogen embrittlement is clear for specimens in the as-received condition as well, as demonstrated by values in Table 2 and the brittle quasi-cleavage fracture mode shown in Fig. 6(a).

## 5. Conclusions

SMSS specimens subjected to three commonly used heat treatment processes had a similar fracture behavior in tests in air, showing a ductile fracture mode by microvoid coalescence. It was shown that samples which were heat-treated to a condition where relatively lower δ-ferrite and higher retained austenite contents were obtained exhibited a slightly more ductile fracture mode than the other conditions, with higher $K_{apparent}$ values. When specimens were step loaded in a synthetic seawater environment under cathodic overprotection, hydrogen embrittlement led to a clear transition to a more brittle fracture mode in specimens under all conditions, this being by quasi-cleavage for the as-received condition and predominantly intergranular brittle fracture mode for the heat-treated specimens. Heat-treated specimens also had values of $K$ at fracture which were substantially lower than those obtained for the as-received condition. The intergranular fracture mode and the lower δ-ferrite content of the heat-treated specimens suggest that precipitation of chromium carbides occurred in grain boundaries during the austenitization cycle, which caused sensitization of the area and are also a trap site for hydrogen, thus decreasing considerably the mechanical performance of the material in this environment.

### Acknowledgments

### References

1. P.S. Jackman and H. Everson, Development of New Martensitic Stainless Steels for Octg: The Challenges for the Steelmaker and the Tubemaker, *Corrosion/1995*, number 89, NACE International, Houston, TX, 1995, p 1–8

2. V. Olden, C. Thaulow, and R. Johnsen, Modelling of Hydrogen Diffusion and Hydrogen Induced Cracking in Supermartensitic and Duplex Stainless Steels, *Mater. Des.*, 2008, **29**, p 1934–1948

3. Y. Miyata, M. Kimura, and T. Koseki, Martensitic Stainless Steel Seamless Linepipe with Superior Weldability and $CO_2$ Corrosion Resistance, *Corrosion/1997*, number 19, NACE International, Houston, TX, 1997, p 1–8

4. P.D. Bilmes, M. Solari, and C.L. Llorente, Characteristics and Effects of Austenite Resulting from Tempering of 13CrNiMo Martensitic Steel Weld Metals, *Mater. Charact.*, 2001, **46**, p 285–296

5. C.A.D. Rodrigues, P.L.D. Lorenzo, A. Sokolowski, C.A. Barbosa, and J.M.D.A. Rollo, Titanium and Molybdenum Content in Supermartensitic Stainless Steel, *Mater. Sci. Eng. A*, 2007, **460–461**, p 149–152

6. K. Kondo, M. Ueda, K. Ogawa, H. Amaya, H. Hirata, H. Takabe, and Y. Miyazaki, Alloy Design of Super 13Cr Martensitic Stainless Steel (Development of Super 13Cr Martensitic Stainless Steel for Line Pipe), *Proceedings of the Conference in Supermartensitic Stainless Steels*, number 03098, NACE International, Houston, TX, 1999, p 11–18

7. N. Anselmo, J.E. May, N.A. Mariano, P.A.P. Nascente, and S.E. Kuri, Corrosion Behavior of Supermartensitic Stainless Steel in Aerated and $CO_2$-Saturated Synthetic Seawater, *Mater. Sci. Eng. A*, 2006, **428**(1–2), p 73–79

8. G. Pieta, "Avaliação da tenacidade à fratura de um aço inoxidável supermartensítico submetido à proteção catódica em água do mar (Evaluation of the Fracture Toughness of a SMSS Subjected to Cathodic Protection in Sea Water)," Ph.D. Thesis, PPGEM-UFRGS, 2009

9. T. Boellinghaus, H. Hoffmeister, J. Klemme, and H. Alzer, Finite Element Calculation of Hydrogen Uptake and Diffusion in Martensitic Stainless Steel Welds, *Corrosion/1999*, number 609, NACE International, Houston, TX, 1999, p 1–8

10. D.M. Seeger and T. Boellinghaus, Hydrogen Permeation in Supermartensitic Stainless Steels Exposed to Realistic Formation Water Compositions, *Corrosion/2003*, number 03098, NACE International, Houston, TX, 2003, p 1–8

11. P. Bala Srinivasan, S.W. Sharkawy, and W. Dietzel, Environmental Cracking Behavior of Submerged Arc-Welded Supermartensitic Stainless Steel Weldments, *Mater. Sci. Eng. A*, 2004, **385**(2), p 6–12

12. S. Olsen and S.M. Hesjevik, Hydrogen Embrittlement from Cathodic Protection on Supermartensitic Stainless Steels, *Corrosion/2004*, number 04546, NACE International, Houston, TX, 2004, p 1–8

13. C. Lindley and W.J. Rudd, Influence of the Level of Cathodic Protection on the Corrosion Fatigue Properties of High-Strength Welded Joints, *Marine Struct.*, 2001, **14**, p 397–416

14. F. Ebrahimi and H.K. Seo, Ductile Crack Initiation in Steels, *Acta Mater.*, 1996, **44**(2), p 831–843

15. "Standard Test Method for Plane-Strain Fracture Toughness of Metallic Materials," American Society of Testing and Materials ASTM E399-90, 1990

16. B.D. Cullity, *Elements of X-Ray Diffraction*, Addison-Wesley, CA, 1978

17. Z. Yu, X. Xu, L. Wang, J. Qiang, and Z. Hei, Structural Characteristics of Low Temperature Plasma-Nitrided Layers on AISI, 304 Stainless Steel with an α′-Martensite Layer, *Surf. Coat. Technol.*, 2002, **153**, p 125–130

18. "Standard Test Method for Crack-Tip Opening Displacement (CTOD) Fracture Toughness Measurement," American Society of Testing and Materials ASTM E1290-99, 1999

19. "Standard Practice for the Preparation of Substitute Ocean Water," American Society of Testing and Materials ASTM D1141-98, 2008

20. G. Roznovska, V. Vodarek, A. Korcak, and M. Tvrdy, Transactions of the VSB—Technical University of Ostrava, *Mech. Ser.*, 2005, **48**(1), p 225–231

21. K. Kondo, K. Ogawa, H. Amaya, M. Ueda, and H. Ohtani, Development of Weldable Super 13Cr Martensitic Stainless Steel for Flowline, *Proceedings of The Twelfth International Offshore and Polar Engineering Conference*, May 26-31, Kitakyushu, Japan, 2002, p 303–311

22. "Standard Test Method for Measurement of Hydrogen Embrittlement Threshold in Steel by the Incremental Step Loading Technique," American Society of Testing and Materials ASTM F1624-06, 2006

23. D. Broek, *Elementary Engineering Fracture Mechanics*, Martinus Nijhoff, The Hague, Netherlands, 1982

24. D. Carrouge, "Transformations in Supermartensitic Stainless Steels," Ph.D. Thesis, University of Cambridge, 2002

25. E. Viyanit, "Numerical Simulation of Hydrogen Assisted Cracking in Supermartensitic Stainless Steel Welds," Ph.D. Thesis, University of London, 2005

26. J.Y. Park and Y.S. Park, The Effects of Heat-Treatment Parameters on Corrosion Resistance and Phase Transformations of 14Cr3Mo Martensitic Stainless Steel, *Mater. Sci. Eng. A*, 2007, **449–451**, p 1131–1134

27. H. Nakamichi, K. Sato, M. Miyata, and K. Masamura, Quantitative Analysis of Cr-Depleted Zone Morphology in Low Carbon Martensitic Stainless Steel Using Fe-(S)TEM, *Corros. Sci.*, 2008, **50**, p 309–315

28. P. Woolling, Understanding and Avoiding Intergranular Stress Corrosion Cracking of Welded Supermartensitic Stainless Steel, *Corrosion/2004*, number 07094, NACE International, Houston, TX, 2004, p 1–8

29. J.G. Gonzalez-Rodriguez, G. Bahena-Martinez, and V.M. Salinas-Bravo, Effect of Heat Treatment on the Stress Corrosion Cracking Behaviour of 403 Stainless Steel in NaCl at 958 °C, *Mater. Lett.*, 2000, **43**, p 208–214